Light activation of Orange Carotenoid Protein reveals initial C8'-C7' double bond *trans*/*cis* isomerization

V.U. Chukhutsina*, J.M. Baxter*, A. Fadini*, R.M. Morgan*, M.A. Pope*, K. Maghlaoui*, C. Orr#, A.Wagner#, J.J. van Thor*

*Department of Life Sciences, Imperial College London, London SW7 2AZ, United Kingdom
Diamond Light Source, Harwell Science and Innovation Campus, Didcot OX11 0DE, United Kingdom

Abstract

Orange Carotenoid protein (OCP) is the only known photoreceptor which uses carotenoid for its activation[1,2]. It is found exclusively in cyanobacteria, where it functions to control light-harvesting of the photosynthetic machinery. However, the photochemical reactions and structural dynamics of this unique photosensing process are not yet resolved. We present time-resolved crystal structures at second-to-minute delays under bright illumination, capturing the early photoproduct and structures of the subsequent reaction intermediates. The first stable photoproduct shows carotenoid *trans*/*cis* isomerization at the C7'-C8'double bond and structural changes in the N-terminal domain with minute timescale kinetics. These are followed by a thermally-driven *cis*/*trans* isomerization that recovers to the dark state carotenoid configuration. Structural changes propagate to the C-terminal domain, resulting, at later time, in the H-bond rupture of the carotenoid keto group with protein residues. The isomerization and its transient nature are confirmed in OCP crystals and solution by FTIR and UV/Vis spectroscopy. This study reveals the isomerization of the carotenoid and subsequent thermal structural reactions as the basis of OCP photoreception. Understanding and potentially controlling the OCP dynamics offers the prospect of novel applications in biomass engineering[3] as well as in optogenetics and bioimaging.

Main text

Carotenoids are found in plants, algae, and microorganisms and constitute the most widely spread group of pigments[4]. Carotenoids are isoprenoids made-up of a central carbon chain of alternating single and double bonds with unique photochemical properties. The S0-S1 electronic transition is optically forbidden in carotenoids and light absorption occurs through the intense S0-S2 transition[5] which is responsible for their yellow, orange and red colours. After light absorption, the S1 dark state is populated through internal conversion, which then relaxes with a picosecond lifetime[6]. The structure and conformation of carotenoids determine the energy landscape of their electronic states and, as a result, their biological functions. Carotenoid chromophores function as key photosynthetic regulators of biomass production[3,7] when their S1 states act as efficient quenchers of chlorophyll excited states[8,9]. Furthermore, carotenoid excited states also act as energy donors in photosynthetic light-harvesting[6] as well as photoreceptors in light-signalling[10]. The structural and molecular basis for the diverse biological functions of carotenoid chromophores is of high importance and is necessary to fully understand in order to gain control of these processes. The carotenoid canthaxanthin (CAN) bound to the Orange Carotenoid Protein is responsible for a light signalling function. OCP undergoes a photocycle[1] in which the keto-carotenoid also plays several different roles: in the

inactive state (orange, OCP^O, Fig 1a), it senses blue-green light to initiate its photocycle, resulting in a final product that has undergone substantial structural conformational changes and exhibits distinct separation of the two OCP domains, namely, the all-helical N-terminal domain (NTD) and an α/β-fold C-terminal domain (CTD)[11]. In the active state, following OCP^R (red state) binding to the cyanobacterial light-harvesting antenna, the keto-carotenoid dissipates excess absorbed light energy, a vital process for cyanobacterial survival in turbulent waters[12,15].

The mechanism and primary photochemical reaction of the keto-carotenoid that triggers this OCP^O-OCP^R conversion is currently debated and, therefore, requires structural evidence[10,12]. It has been argued that OCP photoactivation is initiated by H-bond rupture between the 4-keto group of the β1-ring and neighbouring residues Y201 and W288.[13–19] Several different proposals have been made for the primary photochemistry resulting in this particular H-bond rupture: (1) a charge transfer state[20]; (2) a shift in keto–enol equilibrium[16]; (3) a transfer of vibrational energy from the carotenoid to the protein leading to the H-bond rupture[21], similar to H-bond rupture in bacteriorhodopsin [22]; (4) a structurally distorted form of the carotenoid in the S1 state characterized by increased carotenoid planarity[17]; (5) a photoinduced s-isomerization of the C6−C7 single bond, flipping the orientation of the β1-ring by 90°[13]. Support for s-isomerization in OCP stemmed from the X-ray structure of the isolated NTD (also known as red carotenoid protein, RCP), in which the keto-carotenoid was present in a C6−C7 s-*cis* conformation[13], and frequency calculations showing agreement between a C6−C7 s-*cis* conformation and OCP^R Resonance Raman data[22]. However, the hypothesis for s-isomerization in OCP^R is not consistent with recent infra-red (IR) anisotropy observations[17]. A recent study of the fluorescence spectra and yields of OCP^O with different carotenoids suggested that the mechanism of OCP photoactivation does not involve the keto group of the β1 ring but includes out-of-plane motions of the β2 ring[23]. Here we show time resolved crystallographic and spectroscopic evidence which resolve the initial photoproducts and subsequent structural propagation in the activation process.

Figure 1c shows the light induced absorption changes measured in crystals and solutions of OCP confirming that the same photoactivation reactions proceed in both cases. In contrast to a previous crystallographic investigation of OCP photoactivation[16], we observe that the absorbance spectra of OCP^O in solution and in crystals are nearly identical (Fig 1b), thereby providing evidence for the same electronic structure of the reactant and product states of the carotenoid in both crystals and solution. Illumination of crystals with 410 nm light and 3.5 $mWcm^{-2}$ power density causes a significant spectral red-shift of 25 nm due to OCP^O-OCP^R conversion within 5 min on average (Fig 1b insert).

An early reaction intermediate was captured by intense illumination and cryo-trapping of OCP crystals, using time delays according to the overall rate kinetics determined from spectroscopy. The crystal structure and carotenoid conformation was determined at 1.3 Å resolution for the dark state (OCP_{Dark}, Fig 1a) and was found to be in good agreement with those reported in previous X-ray studies[1,13,14,16] (Extended Data Table 1). The data furthermore supports identification of glycerol, acetate, Cl^- and 440 water molecules in the crystal structure (Extended Data Fig 1, Extended Data Table 2-3). In addition to OCP_{Dark}, X-ray crystallography data was collected of four illuminated structural intermediates I1, I2, I3 and I4 corresponding

to 1 min, 2 min, 5 min and 10 min of illumination. Data collection and refinement statistics were comparable to that of the OCP_{Dark} reference data. Q-weighted F_{Light}–F_{Dark} difference electron density (DED) maps[24] and coordinates refined to extrapolated structure factors for the light condition (see Materials and Methods, Extended Data Fig 2) for CAN are presented in Fig 1c. The OCP_{I1} dataset with 1 minute illumination reveals isomerization of CAN around the C8'-C7' double bond as the early step of activation (Fig 1 c-d, Extended Data Fig 3). The isomerization-related DED signals are also detected in OCP_{I2}, though less pronounced compared to OCP_{I1}. In contrast to OCP_{I1} the refined coordinates of OCP_{I2} supports only a minor population of the C8'-C7'cis state and the C8'-C7'trans conformation becomes again the dominant state. The crystallographic observations for the first 2 min of illumination agree with the kinetics determined by spectroscopy and identify the CAN carotenoid isomerization reaction from an all-*trans* to a C8'-C7'-*cis* state which occurs with k_{isom}=0.0263 s^{-1} (Fig 4) as well as the subsequent *cis-trans* thermal relaxation (k_{therm}=0.0062 s^{-1}, Fig 1 d and Fig 4). The isomerization fully decays after 5 min in OCP_{I3} and OCP_{I4} judging from DED maps, 2mFo-DFc maps, and refined coordinates using extrapolated structure factors (Fig 1, Extended Data Table 1).

Occupancy analysis shows that the CAN carotenoid converts from an all-*trans* to a C8'-C7'-*cis* state with complete accumulation of the photoproduct within 1 min of illumination at the experimental light intensity used at ambient temperature. UV/Vis spectroscopy confirms that the rate of accumulation of the first stable photoproduct is proportional to the illumination intensity (Extended Data Fig 4 a-c). Complete thermal relaxation of C8'-C7'-*cis* CAN back to all-*trans* state occurs after 5 min illumination but also in darkness (Extended Data Fig 4 a-c, Supplementary information). In contrast to the current prevailing model [13–19], which proposes a H-bond rupture in CTD as the primary photoproduct of the OCP photocycle, our X-ray data directly demonstrate that a transient C8'-C7'-*cis* state is generated prior to rearrangements in CTD. This finding reveals the molecular activation mechanism that precedes the formation of product states described in the literature. The OCP_{I1} structure is a first example where double bond isomerization of a carotenoid carbon chain regulates the activity or the biological function of a protein.

Photoinduced structural changes occur throughout the OCP protein and propagate in a time-dependent manner. The F_{I1}–F_{Dark} map reproducibly displays differences in three regions (Fig 2, Extended Data Fig 2): in the NTD with the highest DED amplitudes within 6 Å from the CAN β2 ring (Zone 1, Fig 1c), in the N-terminal extension (Zone 2, Fig 1c) and at the interface between the two domains. The DED signals appear in the CTD (Zone 3, Fig 1c, Extended Data Fig 2) with time delays longer than 1 min. In the I2 intermediate (i.e. after 2 min of illumination), the DED signals appear primarily in the region of the CAN binding pocket and subsequently appear along helices of the CTD in the I3 and I4 structures (Fig 1c). Concomitant with the development of DED signals in the CTD, the DED signals in Zones 1 and 2 decay in I3 and I4. These results indicate that NTD is the primary site of action in the OCP light-activation. Therefore, the initiation of photo-sensing in the OCP photocycle involves structural changes in the NTD rather than in the CTD as previously suggested[16].

The structural rearrangements in the intermediates I1, I2, I3 and I4 are analysed in detail following coordinate refinement. Tyrosine Y44 and tryptophan W110 are located in closest

proximity (4 Å) to the C7'-C8' bond in the hydrophobic pocket which also contains the β2-ring of the carotenoid (Fig 3 a). Together with W41, residues Y44 and W110 interact with the carotenoid β2-ring through π-π stacking.[14] In the OCP_{I1} structure, no change of coordinates are observed for W110 compared to OCP_{Dark} but the Y44 sidechain undergoes a rotation by 31° (Fig 3 a). This observation suggests that the Y44 sidechain reacts to C7'-C8' isomerization to trigger structural changes in NTD. The structures of the I1 and I2 intermediates suggest that the repositioning of the Y44 sidechain causes the displacement of multiple amino acids in NTD. These include residues Y111 and G114, which are closest to Y44 and are displaced in OCP_{I1} and OCP_{I2} (Fig 3a). In agreement with our crystallographic observations, previous spectroscopic analysis demonstrated that the Y44S mutation fully inhibits OCP^{O}-OCP^{R} conversion[19]. As a result of repositioning of numerous amino acids in NTD, substantial charge-density redistribution around the β2-ring is expected in OCP_{I1} (Extended Data Fig 4 d-e). These changes are transient and the amino acids return to their original location as in OCP_{Dark} after 5-10 min of continuous illumination (Fig 3 a). Leucine L37, which has been proposed to play an important role in OCP light-activation [23], does not undergo any significant movement upon illumination (Extended Data Fig 5 a). We therefore conclude that C7'-C8' isomerization causes rearrangement of the CAN β2-ring binding pocket in the NTD, which is mediated by contact with Y44.

The rearrangement of the β2-ring binding pocket coincides with further conformational changes within the NTE and the NTD. This affects primarily helices αA-αC and αE - αH, as can be judged from the location of DED signals-(Fig 2). The amplitude of these signals is maximal after a 1 min illumination (F_{I1}–F_{Dark}) followed by a decrease after a 2 min illumination (F_{I3}–F_{Dark}) and complete decay after a 10 min illumination (F_{I4}–F_{Dark}). The conformational rearrangements of the $\alpha A - \alpha C$ and the $\alpha E - \alpha H$ helices affect the hydrogen-bond network by increasing the number of polar contacts in the main backbone of OCP_{I1} by 5% compared to OCP_{Dark}. In OCP_{I1}, 14 new H-bonds are created in the backbone which gradually decay in OCP_{I2}-OCP_{I4} (Extended Data Table 4). These results indicate that, following light-activation, the light-sensing process in OCP is mediated not only by the CAN β2-ring binding pocket but involves the hydrogen-bonding of the whole domain.

The DED signals within a 5 Å radius from the carotenoid at the CTD and NTD interface (Fig 1c) are assigned to the modification of the salt bridge between R155, E244 (Fig 4 b) and the reorganisation of water molecules (Fig 3b, Extended Data Fig 5). The salt bridge rupture between R155 and E244 is already observed in OCP_{I1} and it is noticeable as a increase of the distance between residues E244 and R155 by 1 Å (Fig 3b). The position of R155 is affected by the water molecules HOH41 and HOH46 through H-bonding (Fig 3b, Extended Data Fig 6 a). The positions of HOH41, HOH46, Cl^- anion and other water molecules in the water channels are rearranged during the illumination period (Extended Data Fig 5-6, Fig 3b). In the final illumination product (OCP_{I4}, Fig 3b) the distance between residues E244 and R155 is restored to the original 3 Å distance found in the dark state, suggesting that, although an important event in the initial steps of light activation, salt-bridge rupture may not be a prerequisite for subsequent domain separation. Previously reported FTIR and X-ray protein footprinting results suggested that signal propagation of OCP conformational change is mediated by rearrangement of internal hydrogen bonding networks[11,25]. We complement this knowledge by showing that

salt bridge rupture between R155 and E244, the important precursor of NTD and CTD separation, occurs in the first illumination step (I1) and is controlled by a hydrogen bonding network involving protein-bound water molecules.

In addition, an increase in DED signal intensities in the CTD is observed with increasing illumination time (Zone 3, Fig 1). This is first manifested in CTD amino acids P276, L248, P278 and E244 located at the interface of CTD and NTD (Extended Data Fig 6 a). The DED signals for the CTD (Fig 2) do not represent a complete domain rearrangement but rather a rigid-body motion of the CTD domain in the direction away from the NTD and the dimer interface (Extended Data Fig 6) similar to that previously reported[16]. The increase in distance between W288, Y201 and the keto group of CAN, a suggested prerequisite for H-bond disruption[16], is only observed at longer illumination times (after 5-10 min, Extended Data Fig 6) and only after rearrangement of the NTD binding pocket. Therefore, the H-bond rupture represents a secondary effect caused by domain separation and it is not a photo-driven process as previously proposed [16,17].

Next, we performed FTIR and UV/Vis spectroscopy in solution using the same illumination conditions as for crystals (Figs 1-3) in order to confirm that CAN isomerization is photoinduced (Fig 4) and determine whether the same photoactivation reactions observed in crystals also take place in solution. Fig 4 displays the results from the combined global analysis fits of the UV/Vis and FTIR data. Since the experiment was performed under continuous illumination, the Evolution-Associated Spectra (EAS) components do not represent intrinsic lifetimes of the intermediate states but rather dissected population accumulation rates at given illumination power densities (Extended Data Fig 4 a-c). Four components of spectral regions (EAS1-4) are identified to describe the absorbance changes in both UV/Vis and IR spectra with lifetimes of 13 s, 38 s, 162 s and a steady-state component (infinity). The photocycle kinetics in OCP solution and OCP crystals are very similar (Fig 1B). The contribution of each component in I1-I4 states in Figs 1-3 is as follows: (i) I1 state: EAS1 (3%), EAS2 (40%) and EAS3 (57%), (ii) I2 –EAS2 (13%) and EAS3 (87%), (iii) I3 –EAS2 (2%) and EAS3 (98%) and (iv) I4- EAS3 -100%. Note that the absence of the final component EAS4 in crystals is probably due to crystal packing constraints on side-chain conformational dynamics so it was excluded from the population estimates (see the justification below). The first component (EAS1) exhibits a positive and a negative spectral signature in the visible region (Fig 4a) peaking at 475 nm and 550 nm respectively. It does not show significant IR differences (Fig 3b, Extended Data Fig 4 f). We assign this observation to the conversion of OCP^O into a new intermediate species EAS2. EAS2 (at 38s) has a very similar visible spectrum to OCP^O (t_0 spectra) though it has an increased absorbance at 350 nm (Fig 4a insert). The 350-nm band yields the so-called '*cis*-peak', a characteristic signature of *trans-cis* isomerization in carotenoids[26,27]. The IR spectrum of the corresponding EAS2 component in D_2O buffer shows positive bands in the 1655-1641 cm^{-1} region while exhibiting a negative band at 1540-1550 cm^{-1}(Fig 4b). The positive band corresponds to the amide I signal. The position of the 1542-1550 cm^{-1} bleach is insensitive to D_2O / H_2O exchange and agrees with the frequency of C=C stretches in canthaxanthin [28] and other carotenoids[29]. In carotenoids, the oscillator strength of C=C stretches is known to decrease with isomerization from all-*trans*-to-*cis* conformations[30]. Therefore, the presence of the 1542-1550 cm^{-1} bleach in the EAS2 component agrees very well with its assignment to the

trans-cis CAN isomerization as seen on Fig 1c in I1 and indicates that the process is light-induced. The EAS3 component (162-s, Fig. 4) confirms that isomerization is a transient phenomenon leading to a C7'-C8'-*trans* state in 2.5 min as can be concluded from a decrease of the 1542 cm^{-1} bleach. An additional UV/Vis measurement with a shorter illumination period confirms that the back C7'-C8'*cis-trans* relaxation is thermally driven (Extended Data Fig 4 a). To confirm the FTIR assignments, we also performed harmonic frequency calculations of CAN in the all-*trans* (CAN_{Dark}) and in the C7'-C8'-*cis* (CAN_{I1}) states using the carotenoid coordinates shown in Fig 2 after optimisation using redundant coordinates. The major frequency of the C=C stretches coupled with the C=O stretches in CAN_{Dark} is 1542 cm^{-1}, while in the CAN_{I1} state, its oscillator strength decreases and its frequency redshifts to 1550 cm^{-1}. The resulting calculated difference signal (CAN_{I1}-CAN_{Dark}) is characterized by the 1542 cm^{-1} bleach (Fig 4 c). Our spectroscopic results, supported by frequency calculations, thus confirm that *trans-cis* C8'-C7' isomerization is a light-driven process also occurring in OCP in solution.

The EAS2 component also contains positive amide-I FTIR signals peaking at 1651 cm^{-1} and 1641 cm^{-1} due to a bleaching signal emerging at later stages (EAS3). These signals, assigned to amide-I peaks based on previously reported IR signals of OCP WT and mutants[17], are indicative of H-bond rearrangements which are seen in the OCP_{I1} crystal structure (Extended Data Table 4). The positive amide-I FTIR signals can be assigned to the new polar contacts appearing in OCP_{I1} (EAS2, 38 s, Fig 4b). Negative amide-I FTIR signals in the EAS3 component indicate the loss of these polar contacts as seen in OCP_{I4}.

In agreement with previous studies[17,25,31] the absorption peak at 1651 cm^{-1} is insensitive to D_2O/H_2O exchange, unlike that at 1645 cm^{-1} (Extended Data Fig 4 g, Supplemental Information). We have therefore tentatively assigned the 1651 cm^{-1} and 1641 cm^{-1} (D_2O)/1645 cm^{-1} (H_2O) bands to a buried α-helix and to a solvent exposed α-helix of NTD respectively (see Supplementary Information for the contribution of water molecules to FTIR data).

Contrary to a previous suggestion[25], our data does not support involvement of the C-terminal tail to changes of the 1645cm^{-1} peak, since no structural rearrangements are observed in this region in the crystallographic data corresponding to the same time delays (I1-I2, Fig 2, Extended Data Fig 2 b). In line with the final OCP_{I4} crystal structure, where the CTD translocates away from the NTD without CTD rearrangement, we do not observe CTD characteristic ß-sheet-related FTIR signals in the 1640-1600 cm^{-1} region (Fig 4b). The EAS4 (infinity/steady-state) represents the CTD and NTD complete dissociation[11], which is not observable in the crystallographic data due to the crystal packing constraints (Supplementary Information)[16]. The amide-I FTIR kinetics data and assignments agree well with our crystallographic observations, indicating that the same photoinduced structural rearrangements occur both in OCP solutions and in crystals.

This work provides the structural basis for the initial reaction in OCP light-activation. Our X-ray data demonstrates that the initial photoproduct is the C7'-C8'*cis* CAN carotenoid. UV/Vis and IR spectroscopic studies in combination with harmonic frequency calculations confirm the reaction mechanism in crystals and solution. In response to the light-induced isomerization, structural changes propagate from the NTD to the CTD. The presented evidence shows that the H-bond rupture between the carotenoid and the CTD protein moiety does not initiate light activation but is a secondary event which follows post-isomerization NTD

rearrangement. The discovery of the overall OCP activation mechanism provides for the first time the foundation for gaining control and manipulation of the light regulation function of OCP with potential applications in optogenetics, bioimaging and agriculture.

Main references

1. Kerfeld, C. A. *et al*. The crystal structure of a cyanobacterial water-soluble carotenoid binding protein. *Structure* **11**, 55–65 (2003).
2. Leverenz, R. L. *et al*. A 12 Å carotenoid translocation in a photoswitch associated with cyanobacterial photoprotection. *Science (80-.)*. **348**, 1463–1466 (2015).
3. Kromdijk, J. *et al*. Improving photosynthesis and crop productivity by accelerating recovery from photoprotection. *Science (80-.)*. (2016). doi:10.1126/science.aai8878
4. Maoka, T. Carotenoids as natural functional pigments. *Journal of Natural Medicines* (2020). doi:10.1007/s11418-019-01364-x
5. Polivka, T. & Sundstrom, V. Ultrafast dynamics of carotenoid excited States-from solution to natural and artificial systems. *Chem Rev* **104**, 2021–2071 (2004).
6. Polívka, T. & Frank, H. A. Molecular factors controlling photosynthetic light harvesting by carotenoids. *Acc. Chem. Res*. (2010). doi:10.1021/ar100030m
7. Ruban, A. V *et al*. Identification of a mechanism of photoprotective energy dissipation in higher plants. *Nature* **450**, 575–578 (2007).
8. Liguori, N. *et al*. Different carotenoid conformations have distinct functions in light-harvesting regulation in plants. *Nat. Commun*. (2017). doi:10.1038/s41467-017-02239-z
9. Pascal, A. A. *et al*. Molecular basis of photoprotection and control of photosynthetic light-harvesting. *Nature* **436**, 134–137 (2005).
10. Muzzopappa, F. & Kirilovsky, D. Changing Color for Photoprotection: The Orange Carotenoid Protein. *Trends in Plant Science* (2020). doi:10.1016/j.tplants.2019.09.013
11. Gupta, S. *et al*. Local and global structural drivers for the photoactivation of the orange carotenoid protein. *Proc Natl Acad Sci U S A* **112**, E5567-74 (2015).
12. Kirilovsky, D. & Kerfeld, C. A. The Orange Carotenoid Protein: A blue-green light photoactive protein. *Photochem. Photobiol. Sci*. **2**, 1135–1143 (2013).
13. Leverenz, R. L. *et al*. A 12 Å carotenoid translocation in a photoswitch associated with cyanobacterial photoprotection. *Science (80-.)*. **348**, 1463–1466 (2015).
14. Wilson, A. *et al*. Structural determinants underlying photoprotection in the photoactive orange carotenoid protein of cyanobacteria. *J. Biol. Chem*. (2010). doi:10.1074/jbc.M110.115709
15. Wilson, A. *et al*. The essential role of the N-terminal domain of the orange carotenoid protein in cyanobacterial photoprotection: Importance of a positive charge for phycobilisome binding. *Plant Cell* (2012). doi:10.1105/tpc.112.096909
16. Bandara, S. *et al*. Photoactivation mechanism of a carotenoid-based photoreceptor. *Proc Natl Acad Sci U S A* **114**, 6286–6291 (2017).
17. Konold, P. E. *et al*. Photoactivation Mechanism, Timing of Protein Secondary Structure Dynamics and Carotenoid Translocation in the Orange Carotenoid Protein. *J. Am. Chem. Soc*. (2019). doi:10.1021/jacs.8b11373
18. Bondanza, M., Cupellini, L., Lipparini, F. & Mennucci, B. The Multiple Roles of the Protein in the Photoactivation of Orange Carotenoid Protein. *Chem* **6**, 187–203 (2020).
19. Wilson, A., Punginelli, C., Couturier, M., Perreau, F. & Kirilovsky, D. Essential role of two tyrosines and two tryptophans on the photoprotection activity of the Orange Carotenoid Protein. *Biochim. Biophys. Acta-Bioenergetics* **1807**, 293–301 (2011).
20. Yaroshevich, I. A. *et al*. Role of hydrogen bond alternation and charge transfer states in photoactivation of the Orange Carotenoid Protein. *Commun. Biol*. (2021). doi:10.1038/s42003-021-02022-3
21. Wei, T., Balevičius, V., Polívka, T., Ruban, A. V. & Duffy, C. D. P. How carotenoid distortions may determine optical properties: Lessons from the orange carotenoid protein. *Phys. Chem. Chem. Phys*. (2019). doi:10.1039/c9cp03574e

22. Nogly, P. *et al*. Retinal isomerization in bacteriorhodopsin captured by a femtosecond x-ray laser. *Science (80-.)*. (2018). doi:10.1126/science.aat0094
23. Gurchiek, J. K. *et al*. Fluorescence and Excited-State Conformational Dynamics of the Orange Carotenoid Protein. *J. Phys. Chem. B* (2018). doi:10.1021/acs.jpcb.7b09435
24. Ursby, T. & Bourgeois, D. Improved Estimation of Structure-Factor Difference Amplitudes from Poorly Accurate Data. *Acta Crystallogr. Sect. A Found. Crystallogr.* (1997). doi:10.1107/S0108767397004522
25. Mezzetti, A. *et al*. Two-Step Structural Changes in Orange Carotenoid Protein Photoactivation Revealed by Time-Resolved Fourier Transform Infrared Spectroscopy. *J. Phys. Chem. B* (2019). doi:10.1021/acs.jpcb.9b01242
26. Zechmeister, L. & Polgár, A. cis-trans Isomerization and Spectral Characteristics of Carotenoids and some Related Compounds. *J. Am. Chem. Soc.* (1943). doi:10.1021/ja01248a025
27. Polgár, A. & Zechmeister, L. Action of Cold Concentrated Hydriodic Acid on Carotenes: Structure and cis-trans-Isomerization of Some Reaction Products. *J. Am. Chem. Soc.* (1943). doi:10.1021/ja01248a026
28. Philip, T. & Francis, F. J. Isolation and chemical properties of capsanthin and derivatives. *J. Food Sci.* **36**, 823–827 (1971).
29. Schlücker, S., Szeghalmi, A., Schmitt, M., Popp, J. & Kiefer, W. Density functional and vibrational spectroscopic analysis of β-carotene. *J. Raman Spectrosc.* (2003). doi:10.1002/jrs.1013
30. Berezin, K. V. & Nechaev, V. V. Calculation of the IR spectrum and the molecular structure of β-carotene. *J. Appl. Spectrosc.* (2005). doi:10.1007/s10812-005-0049-x
31. Wilson, A. *et al*. A photoactive carotenoid protein acting as light intensity sensor. *Proc. Natl. Acad. Sci. U. S. A.* (2008). doi:10.1073/pnas.0804636105
32. Wickstrand, C. *et al*. A tool for visualizing protein motions in time-resolved crystallography. *Struct. Dyn.* (2020). doi:10.1063/1.5126921

Figure legends

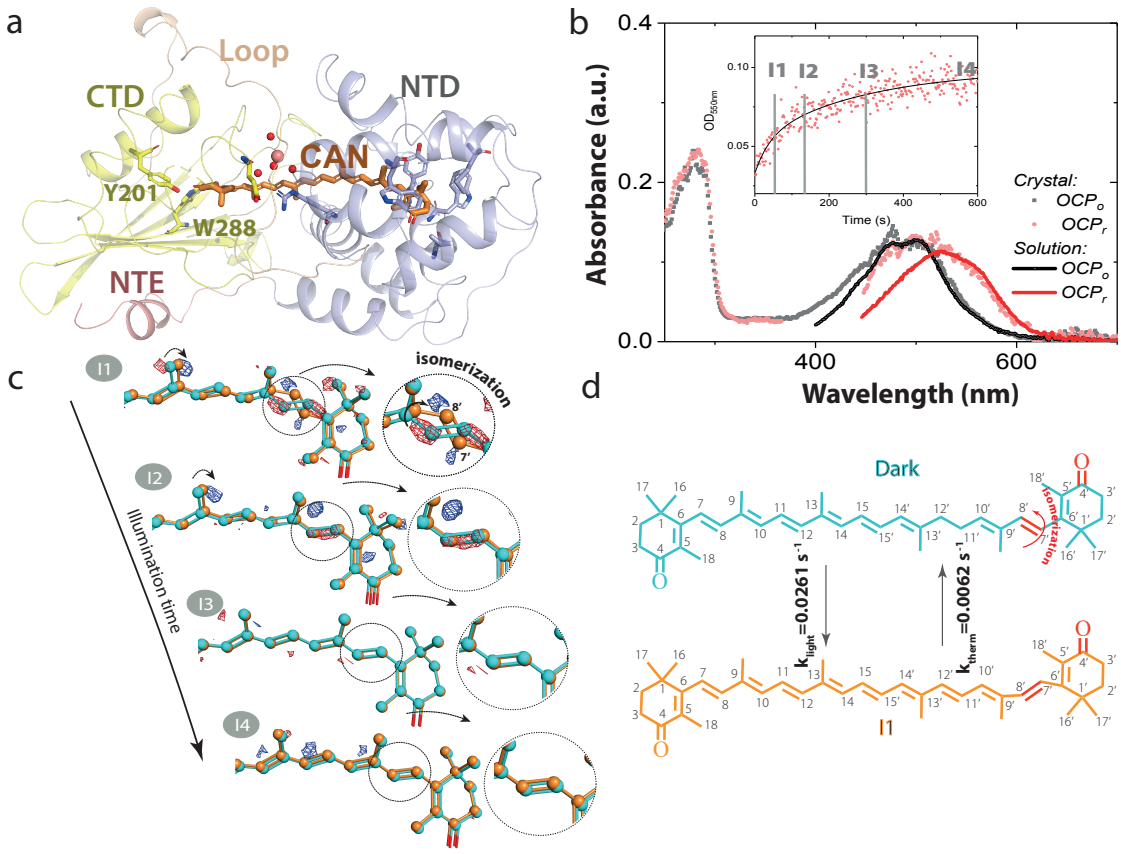

Fig. 1: Canthaxanthin C8'-C7' *trans*-to-*cis* isomerization triggers OCP light activation (a) Structure of OCP_{CAN} in the 'dark' state displaying the C-terminal domain (CTD, yellow colour), N-terminal domain (NTD, blue colour), N-terminal extension (NTE, salmon colour) and loop (wheat colour). The canthaxanthin (CAN) carotenoid is embedded between the two domains. Cl^- (pink sphere) is resolved in the CTD where it coordinates four water molecules (red spheres) through ion-dipole interactions at distances of 3.0-4.0 Å. The closest CAN carbon (C12) is at 4.1 Å distance (Extended Data Fig 1). (b) Absorbance changes of OCP in solution (solid lines) and crystalline state (dotted lines) upon illumination. Inactive state OCP^O and active state OCP^R are shown in black/gray and red/pink respectively. Insert: Absorbance changes (pink dots) in the crystalline state detected at 550 nm upon 10 min of illumination with violet light (at 410 nm with 3.5 mWcm^{-2} power). Black line represents double exponential fit of the curve ($Y = A_1 e^{\frac{x}{t1}} + A_2 e^{\frac{x}{t2}}$, where A_1=0.02, t_1=38 s and A_2=0.44, t_2 = 291 s. In comparison to solution measurements, the OCP^R spectrum maximum in crystals is blue-shifted by 5 nm and has slightly higher absorption in the 470-500 nm region probably due to conformational constraints imposed by the crystal packing which may prevent full separation of the CTD and NTD domains[11].
(c) Difference electron density (DED) maps (blue/red at ±3.0σ) were obtained for the four states: (I1) 1 min (F_{I1}– F_{Dark}), (I2) 2 min (F_{I2}– F_{Dark}), (I3) 5 min (F_{I3}– F_{Dark}), (I4)10 min (F_{I4}– F_{Dark}). Carotenoid coordinates of dark (OCP_{Dark}) and light states (OCP_{I1-I4}) are represented by cyan and orange lines respectively. Arrow in the insert in l1 state indicates carotenoid movement during illumination. (d) All-*trans* CAN is present in OCP_{Dark} while C8'-C7' *cis* conformation is observed in OCP_{I1}. The latter thermally recovers back to all-*trans* state with prolonged illumination time (after 2-5 min).

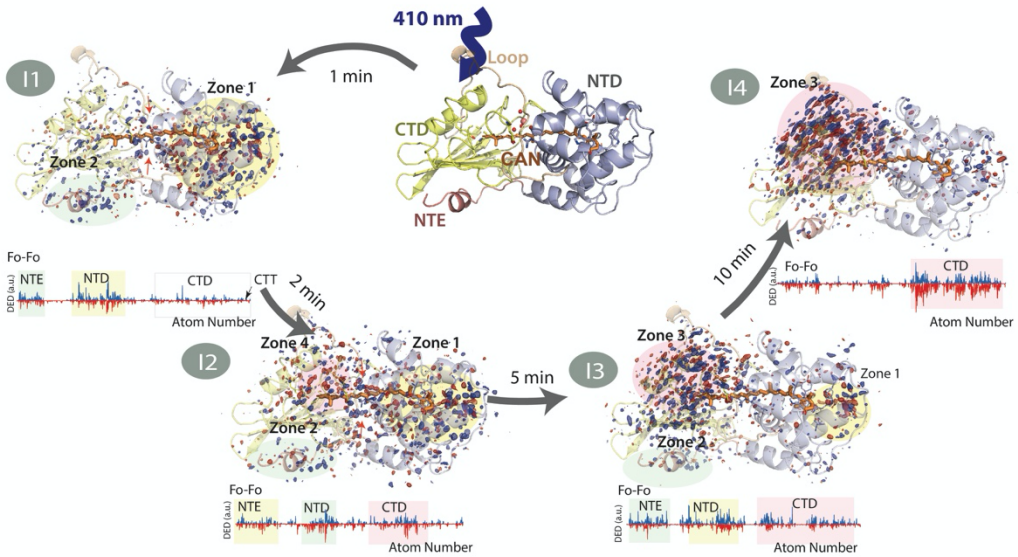

Fig. 2: Overall structural effect of illumination on OCP structure. Datasets from which all images are derived (Dark, I1-I4) have a resolution of 1.3 -1.4 Å (Supplementary Information) and time points at which crystals were cryo-trapped are indicated for I1-I4. (I1- I4, upper panel) F_0- F_0 Difference electron density (DED) maps (blue/red at ±3.5σ) for the four states shown below each corresponding structure: (I1) 1 min (F_{I1}– F_{Dark}), (I2) 2 min (F_{I2}– F_{Dark}), (I3) 5 min (F_{I3}– F_{Dark}) and (I4) 10 min (F_{I4}– F_{Dark}). The DED signals are localized in the 3 major areas: *zone 1*: NTD; *zone 2*: NTE; *zone 3*: Alpha- helices in CTD. Note that some DED signals are observed at the interface between the two domains (red arrows in I1 and I2) while the C-terminal tail (CTT) does not exhibit any noticeable DED signal. See main text for explanations. (I1-I4, lower panel) DED signals are also shown as the sequential integrated signals[32] around each atom in the protein chain.

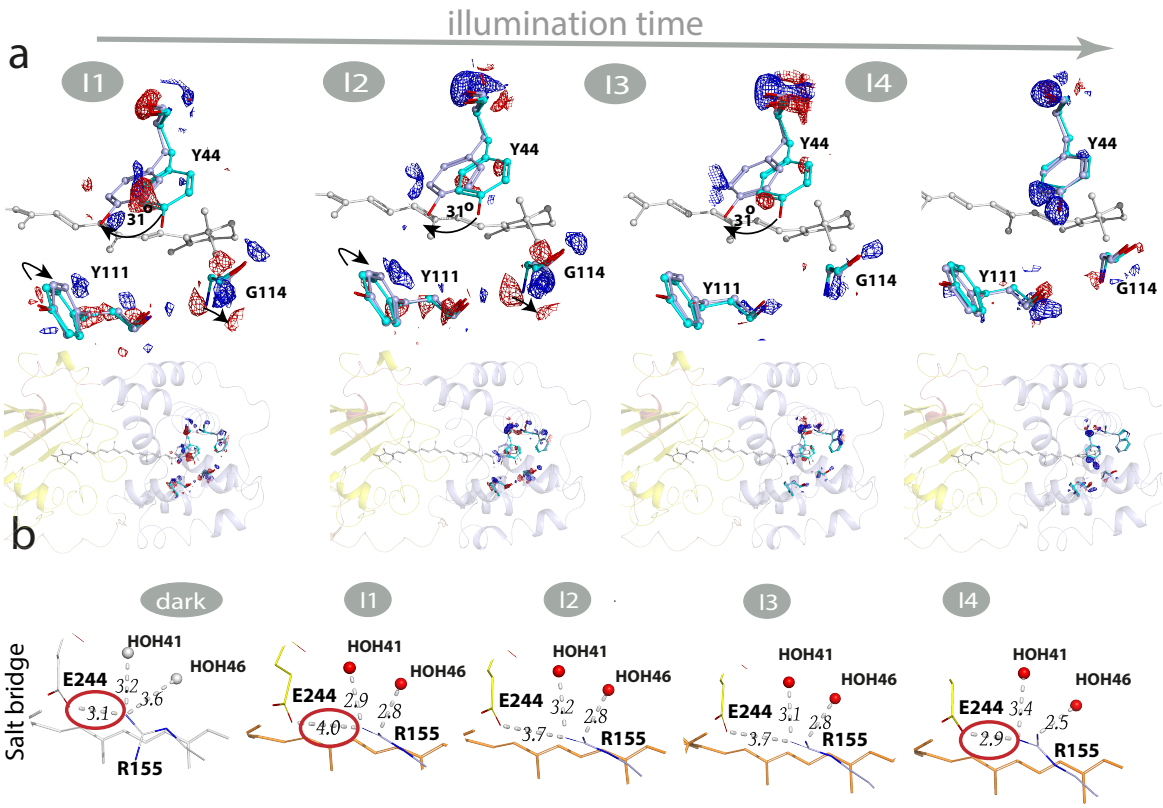

Fig. 3: OCP structural changes around C8'-C7' double bond in I1-I4 states upon illumination (a) Dark state coordinates are represented by cyan sticks while light state coordinates are represented by blue (NTD) and grey (CAN) sticks. Difference electron density (DED) F_{Light}–F_{Dark} are shown with blue/red mesh at ±3.0σ). (b) Changes in the salt bridge formed between residues E244 and R155.

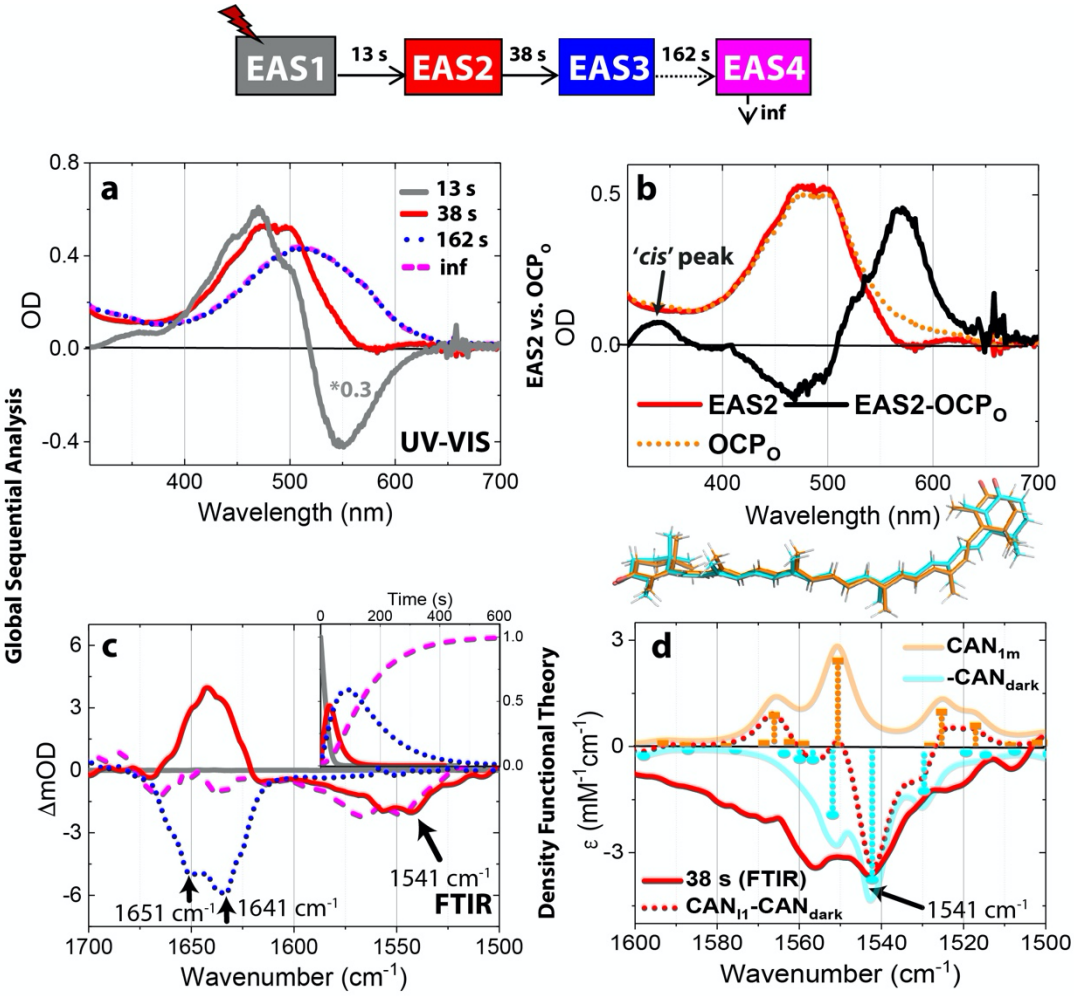

Fig. 4: Spectroscopic evidence for CAN C8'-C7' *trans*-to-*cis* isomerization in OCP in solution (a, c). Results of the simultaneous global fit of UV-VIS (a) and FTIR (c) data upon 10 min of illumination. The kinetic model used for the fit is shown on top of the panel with the respective lifetime for each transition between intermediates. The same colour code is used for the corresponding EAS components in panels a-b. Refer to the main text for an explanation of the relationship between the resolved EAS and the illuminated structural intermediates I1-I4 (Fig 1-3). (a) UV-VIS EAS. (b) EAS2 component was compared to the original OCP^O spectrum before illumination at t_0. (c) FTIR EAS (in D_2O); FTIR (in H_2O) is shown in Extended Data Fig 4 f-g. Insert: Relative concentration profiles for each EAS. (d) Theoretical IR frequencies and intensities were calculated using Harmonic frequency calculations (HFC) at the B3LYP/6-311+G level. IR values were calculated for CAN in the two (CAN_{Dark} and CAN_{I1}) states using CAN coordinates extracted from the extrapolated maps. Theoretical IR frequencies and calculated FTIR spectra are presented by sticks and solid lines respectively. Optimized CAN coordinates from HFC are shown on top of the panel. CAN_{I1}-CAN_{Dark} (grey line) obtained from HFC agree with the 1542 cm^{-1} bleach from the 38-s EAS2 (black line).

Methods

OCP expression

The OCP-encoding gene slr1963 from Synechocystis PCC 6803 was inserted between the NdeI/XhoI sites in the pET28 vector resulting in OCP-pET28 plasmid carrying G-S-S 6X His Tag-OCP at the NTD. To promote canthaxanthin (CAN) incorporation in vivo, the OCP-pET28 plasmid was co-expressed with pAC-CANTHipi plasmid (gift from Francis X Cunningham Jr, Addgene plasmid # 53301; http://n2t.net/addgene:53301; RRID:Addgene_53301). The transformed cells were then grown in the presence of kanamycin (25 μM/ml) and chloramphenicol (25 μM/ mL). Induction was carried out in LB medium at 37 °C for 3-4 hours until the optical density at 600 nm (OD_{600}) of 0.6-0.8 was reached. Then 0.2 mM IPTG was added to trigger OCP expression and the culture was grown for 16-18 hours at 26 °C before harvesting the next day. After IPTG addition, E.coli cells were grown in the dark to prevent any OCP^O-OCP^R conversion. Cells were harvested and pelleted by centrifugation for 15 minutes at 5,000 x g at 4°C and were subsequently stored at -20 °C.

OCP purification

Cell pellets were thawed and re-suspended in lysis buffer (40 mM Tris pH 8, 300 mM NaCl and 10 % glycerol) supplemented with DNase I (0.1 mg/ml) (Roche) and protease inhibitors (1 tablet per 100ml) (Sigma) prior to cell disruption. All purification steps were carried out at 4 °C. Cell lysis was performed with two passes in a cell disrupter (Constant Systems Ltd.) at 40 kpsi. Broken cells then underwent ultra-centrifugation at 142,000 x g for 60 minutes before collecting the cell free extract and incubating it with pre-equilibrated HisTrap Ni^{2+} resin (GE Healthcare) in a 3:1 volume ratio for 2 hours under gentle shaking. Once the slurry was poured in a glass column, His-tagged OCP was washed with five column volumes (CV) of lysis buffer (wash 1) followed by three CV of lysis buffer supplement with 20mM imidazole (wash 2). The protein was washed off with elution buffer (40 mM Tris pH 8, , 300 mM NaCl, 10 % glycerol, and 200 mM imidazole) (Supplementary Fig 18 a). Holo-OCP was subsequently separated from apo-OCP using anion exchange chromatography (DEAE 650 M) (Tosoh, Japan) by performing a 0-100 mM NaCl linear gradient, (Supplementary Fig 18 b). The concertation of Holo-OCP was determined using the maximum extinction coefficient of CAN (118,000 $M^{-1}\cdot cm^{-1}$) [1,2] and the known 1:1 binding stoichiometry of CAN:OCP.

Protein crystallization

OCP was washed with washing buffer (40 mM Tris pH 8, 10 % glycerol) prior to crystallization using the sitting drop vapor diffusion method as follow. 2 µL of OCP at 3 mg/mL was mixed with 1 µL of reservoir solution (100 mM sodium acetate pH 4.5, 10 % poly-ethylene glycol 20,000, 3 % glycerol) and the drops were left to equilibrate at 20 °C for 5 days. Cubic crystals were flash frozen in liquid nitrogen after being transferred to a cryoprotectant solution consisting of the crystallization solution with 30% glycerol.

Absorbance measurements

Crystal pancakes

Slurries of OCP crystals were pelleted at 1,000 x g and 4°C for 2 minutes and the supernatant removed. Pellets were scooped out and squeezed between two siliconized microscope

coverslips using a micrometre to apply controlled force before sealing the edges with superglue. This process ensured the production of a pancake of crystalline matter with a reasonably uniform OD at 410 nm. The final OD_{410} was typically around 0.2-0.3 Illumination was provided by a 10W 410nm Purple COB LED generating 100mW of 410 nm light at the interaction area. The same LED with similar power was used for illumination of single crystals before flash freezing.

Solutions

UV-VIS measurements were collected using an Agilent 8453 spectrophotometer. Samples with an $OD_{500} = 0.4$ were used in a 1 cm light path quartz cuvette. Samples were kept at 20 °C and illuminated with a 405 nm laser (100mW) for 10 min. Absorbance changes were collected at 0.5 s intervals .

FTIR measurements

Fourier-transform infrared (FTIR) spectra were recorded at a 1 cm^{-1} resolution using a Bio-Rad FTS 175C FT-IR spectrophotometer equipped with a mercury cadmium telluride (MCT) detector. Before measurements the instrument was purged with CO_2-free dry air for 120 min. Absorption spectra were collected in the region between 1700 and 1500 cm^{-1}. For FTIR measurements, OCP in its original buffer (40 mM Tris pH 8, 10 % glycerol) was exchanged into either H_2O (40mM Tris pH 8) or D_2O (40mM Tris pD 8) based buffers. 10 μL of sample previously concentrated to the maximum achievable concentration was placed into the Harrick cell fitted with a 6 μm spacer to obtain an OD_{500} around0.2. First, FTIR was measured in a dark-adapted (non-illuminated) state consisting of 2000 interferograms. The sample was then illuminated at 405 nm with a 100mW laser. Each FTIR spectrum containing 100 interferograms was recorded in 38 seconds. A total of 16 spectra were collected sequentially for about 10 min after the onset of illumination.

Global fit of spectroscopic data

The obtained absorbance changes were analysed globally using Glotaran software[3] and the methodology described in [4]. The unbranched, unidirectional, so-called sequential model (EAS1->EAS2>. . .>$EASn_{comp}$) was used, where EAS stands for Evolution Associated Spectra. During the global analysis UV-VIS and FTIR datasets (both D_2O and H_2O) were linked together. The unbranched and unidirectional, so-called sequential model (EAS1->EAS2>. . .>$EASn_{comp}$) was used, where EAS stands for Evolution Associated Spectra. During the global analysis, UV-VIS and FTIR datasets in both D_2O and H_2O buffers were linked together.

X-ray crystallography and refinement

All X-ray diffraction data collection was carried out at i03 and i04 beamlines (Diamond Light Source, UK). OCP crystals belonged to the $P3_221$ space group with a = 82.5 Å, b = 82.5 Å, and c = 87.3 Å. Diffraction data were integrated through xia2 pipeline with DIALS[5]. The structures were solved by molecular replacement with MOLREP [6] using a starting model based on the PDB ID 4XB5. Refinement was performed with REFMAC[7] alternating with / model building using 2Fo-Fc and Fo-Fc maps visualized in COOT[8]. The final model contains one OCP molecule in the asymmetric unit. Statistics for diffraction data collection, structure determination and refinement are summarized in Table S4.
Difference electron density (DED) maps, calculated for various dark datasets (F_{Dark}–F_{Dark})

reveal no map features, indicating that the different "dark" structures are identical and do not exhibit any spatial arrangement differences as expected (Extended Data Fig 2 a). In the illumination experiments, datasets from crystals were obtained following 1 min minute (I1), 2 minutes (I2), 5 minutes (I3) and 10 minutes of illumination (I4) at RT prior to flash freezing in liquid nitrogen. DED maps were generated using using Q-weighted method (see below). In all four cases, the obtained difference maps in different states are highly reproducible (Extended Data Fig 2). The results indicate that the signals must be generated by actual biological phenomenon during OCP light-activation and do not arise from statistical noise. Similar difference signals were also obtained using phenix.fobs_minus_fobs_map method. Figures of crystal structures and difference maps were visualized using pymol (www.pymol.org). Difference density amplitudes were obtained according to [9].
In short, difference amplitudes $A_j(a_i)$ and difference Fourier electron density maps within spheres of radius 2.0 Å centred upon atom a_i were averaged using a 3 σ cut-off and a 0.5 Å grid spacing.

Extrapolated maps and coordinates
To generate extrapolated maps firstly, DED were calculated using the Fourier transform of weighted difference structure amplitudes based on the Bayesian statistics analysis by Ursby *et. al* [10,11]. For each corresponding structure factor difference (ΔF) between the light (F_L) and dark (F_D) data, a weighted factor (w) was calculated and applied to the difference as implemented in [12–14]. Light, dark and calculated structure factors were combined using CAD and scaled using the anisomorphous option in ScaleIt [11]. This placed each set of structure factors onto a normalised absolute scale compared to the calculated structure factors (F_c calculated using SFALL). The final real-space map was calculated using FFT. Phases from the dark state structure, corresponding to unilluminated OCP crystals were used.[11] To identify small structural changes in the illuminated data, extrapolated electron density maps were generated and extrapolated coordinates then refined to these maps. Difference structure factors were added in a linear combination in multiples of N_{EXT} to the calculated dark structure (F_{Dark}) in order to generate extrapolated structure factors (F_{EXT}). The negative electron density around areas of interest in the protein were then integrated. The point where negative density started to build-up was used to determine a characteristic N_{EXT} value which was then used to generate the final extrapolated structure factors. Coordinates were refined against the extrapolated structure factors using five cycles of rigid body refinement in REFMAC[15] and further real space refinement using COOT[8]. The population transfer (PT) was around 10-20% as can be approximated from the N_{EXT} value ($PT = 200/N_{EXT}$)[14]. The following N_{EXT} values were obtained for the four illuminated states: 22 (OCP_{I1}), 19 (OCP_{I2}), 27 (OCP_{I3}), 12 (OCP_{I4}).

Phasing experiment
The crystals were harvested using LithoLoop (Molecular Dimensions) sample mounts on specialised I23 copper sample assemblies. Data were collected on the long-wavelength beamline I23[16] at Diamond Light Source with X-ray energies of 2.9 keV (λ = 4.28 Å) and 2.8 keV (λ = 4.43 Å) using a semi-cylindrical PILATUS 12M detector (Dectris, CH). These energies were selected as they are above and below the Cl absorption edge (E = 2.82 keV/ λ = 4.39 Å) respectively, thus allowing for Cl identification during analysis of anomalous difference Fourier maps. Sweeps of 360° with an exposure time of 0.1s per 0.1° image were taken using the same crystal. To ensure completeness, two datasets for each energy were collected with the multi-axis goniometer at angles κ=0° and φ=0° and, subsequently, κ=-30° and φ=60°. These datasets were interleaved to mitigate radiation damage effects.

For data processing, data integration was performed with XDS and XSCALE programmes. The origin of the PDB model was corrected using POINTLESS, AIMLESS and MOLREP. Phased anomalous difference Fourier maps were produced using ANODE. A cut-off of 6.0 σ was used to identify sites of anomalous contribution.

Harmonic frequency calculations

The Gaussian 06 software package[17,18] using/and the Becke-3-Lee-Yang-Parr functional [19] were used with the 6-311+ G basis set. Theoretical IR values for frequencies and intensities in CAN were calculated for the three states CAN_{Dark} (Fig 4c), CAN_{I1} (Fig 4c), CAN_{I4} (Extended Data Fig 4 i) and for the RCP structure as reported in [20] (Extended Data Fig 4 j). FTIR spectra were derived from the theoretical IR values using Gaussian program by assigning FWHM withspreading the intensity over a Lorentzian function. The Lorentzian line width for each absorption peak in the calculation was taken to be 4 cm^{-1}. The optimization of molecular geometry was performed with fixing all CAN dihedral angles. As a control, FTIR spectra were also calculated for CAN_{I1} and CAN_{Dark} optimised geometries where dihedral angles were not fixed (Extended Data Fig 4 h). The CAN_{I1}-CAN_{Dark} difference signal in Extended Data Fig 4 h results in a similar bleach observed in Fig 3c but with lower amplitude and a shift to lower wavenumbers.

A scaling factor of 0.97[21–23] was used to convert the calculated theoretical frequencies to FTIR spectra.

Methods references

1. Šesták, Z. Britton, G., Liaaen-Jensen, S., Pfander, H. (ed.): Carotenoids. Handbook. *Photosynthetica* (2004). doi:10.1023/b:phot.0000040641.40049.19
2. *Phytoplankton pigments in oceanography: guidelines to modern methods*. *Phytoplankton pigments in oceanography: guidelines to modern methods* (1997). doi:10.1016/s0031-9422(97)00810-8
3. Snellenburg, J. J., Laptenok, S. P., Seger, R., Mullen, K. M. & van Stokkum, I. H. M. Glotaran: A Java-Based Graphical User Interface for the R Package TIMP. *J. Stat. Softw.* **49**, 1–22 (2012).
4. van Stokkum, I. H. M., Larsen, D. S. & van Grondelle, R. Global and target analysis of time-resolved spectra. *Biochim. Biophys. Acta-Bioenergetics* **1657**, 82–104 (2004).
5. Waterman, D. G. *et al.* The DIALS framework for integration software. *CCP4 Newsl. protein Crystallogr.* (2013).
6. Vagin, A. & Teplyakov, A. MOLREP: An Automated Program for Molecular Replacement. *J. Appl. Crystallogr.* (1997). doi:10.1107/S0021889897006766
7. Vagin, A. A. *et al.* REFMAC5 dictionary: Organization of prior chemical knowledge and guidelines for its use. *Acta Crystallogr. Sect. D Biol. Crystallogr.* (2004). doi:10.1107/S0907444904023510
8. Emsley, P. & Cowtan, K. Coot: Model-building tools for molecular graphics. *Acta Crystallogr. Sect. D Biol. Crystallogr.* (2004). doi:10.1107/S0907444904019158
9. Wickstrand, C. *et al.* A tool for visualizing protein motions in time-resolved crystallography. *Struct. Dyn.* (2020). doi:10.1063/1.5126921
10. Ursby, T. & Bourgeois, D. Improved Estimation of Structure-Factor Difference Amplitudes from Poorly Accurate Data. *Acta Crystallogr. Sect. A Found. Crystallogr.* (1997). doi:10.1107/S0108767397004522
11. Winn, M. D. *et al.* Overview of the CCP4 suite and current developments. *Acta Crystallographica Section D: Biological Crystallography* (2011). doi:10.1107/S0907444910045749
12. Schmidt, M., Rajagopal, S., Ren, Z. & Moffat, K. Application of singular value decomposition to the analysis of time-resolved macromolecular x-ray data. *Biophys. J.* (2003). doi:10.1016/S0006-3495(03)75018-8
13. Ren, Z. *et al.* A molecular movie at 1.8 Å resolution displays the photocycle of photoactive yellow protein, a eubacterial blue-light receptor, from nanoseconds to seconds. *Biochemistry* (2001). doi:10.1021/bi0107142
14. Pandey, S. *et al.* Time-resolved serial femtosecond crystallography at the European XFEL. *Nat. Methods* (2020). doi:10.1038/s41592-019-0628-z
15. Murshudov, G. N. *et al.* REFMAC5 for the refinement of macromolecular crystal structures. *Acta Crystallogr. Sect. D Biol. Crystallogr.* (2011). doi:10.1107/S0907444911001314
16. Wagner, A., Duman, R., Henderson, K. & Mykhaylyk, V. In-vacuum long-wavelength macromolecular crystallography. *Acta Crystallogr. Sect. D Struct. Biol.* (2016). doi:10.1107/S2059798316001078
17. Frisch, M. J. *et al.* Gaussian 09, Revision B.01. *Gaussian 09, Revision B.01, Gaussian, Inc., Wallingford CT* (2009).
18. Becke, A. D. Density-functional thermochemistry. III. The role of exact exchange. *J. Chem. Phys.* (1993). doi:10.1063/1.464913
19. Lee, C., Yang, W. & Parr, R. G. Development of the Colle-Salvetti correlation-energy formula into a functional of the electron density. *Phys. Rev. B* (1988). doi:10.1103/PhysRevB.37.785
20. Leverenz, R. L. *et al.* A 12 Å carotenoid translocation in a photoswitch associated with

cyanobacterial photoprotection. *Science* **348**, 1463–1466 (2015).
21. Macernis, M., Sulskus, J., Malickaja, S., Robert, B. & Valkunas, L. Resonance raman spectra and electronic transitions in carotenoids: A density functional theory study. *J. Phys. Chem. A* (2014). doi:10.1021/jp406449c
22. Wong, M. W. Vibrational frequency prediction using density functional theory. *Chem. Phys. Lett.* (1996). doi:10.1016/0009-2614(96)00483-6
23. Mezzetti, A., Kish, E., Robert, B. & Spezia, R. Assignment of IR bands of isolated and protein-bound Peridinin in its fundamental and triplet state by static FTIR, time-resolved step-scan FTIR and DFT calculations. *J. Mol. Struct.* (2015). doi:10.1016/j.molstruc.2014.11.054

Acknowledgements
The data were collected remotely at Diamond Light Source (BAG proposal number mx17221). This project was supported by the EMBO long-term fellowship (EMBO ALTF 244-2017) and has received funding from the European Union Horizon 2020 research and innovation programme under the Marie Sklodowska-Curie grant (agreement No. 839389) to V.C. This work was supported by the Leverhulme Trust award RPG-2018-372. The crystallisation facility at Imperial College was funded by the BBSRC (BB/D524840/1) and Wellcome Trust (202926/Z/16/Z). We thank Violeta Cordon Preciado for technical assistance.

Author contributions

V.U.C. designed the project. V.U.C. expressed and purified OCP protein, prepared OCP crystals, collected and processed X-ray data and UV-VIS/FTIR data. J.M.B assisted with creating Q-weighted maps and extrapolated coordinates. A.F. and J.J.vT. performed Harmonic Oscillator Calculations. R.M.M. assisted with cryo trapping experiment and X-ray data processing. M.A.P. assisted with the designing of OCP expression system in E.coli, while K.M. provided advice and support in obtaining OCP crystals. C.O. and A.W. performed long wavelength experiments. V.U.C. and J.J.vT. wrote the manuscript with the input from J.B., R.M.M., A.F., C.O. and A.W. J.M.B., R.M.M., A.F., C.O., A.W. and in particular K.M., V.U.C. and J.J.vT. contributed to the review and editing. J.J.vT. supervised the project.

Competing interests
The authors declare no competing interests.
Data and materials availability
Coordinates and structure factors for OCP_{Dark} and I1-I4 states in Fig. 1-3 will be made available via the PDB database.
Correspondence
Correspondence to Jasper van Thor.
Supplementary Information
Supplementary Information is available for this paper.

Extended Data

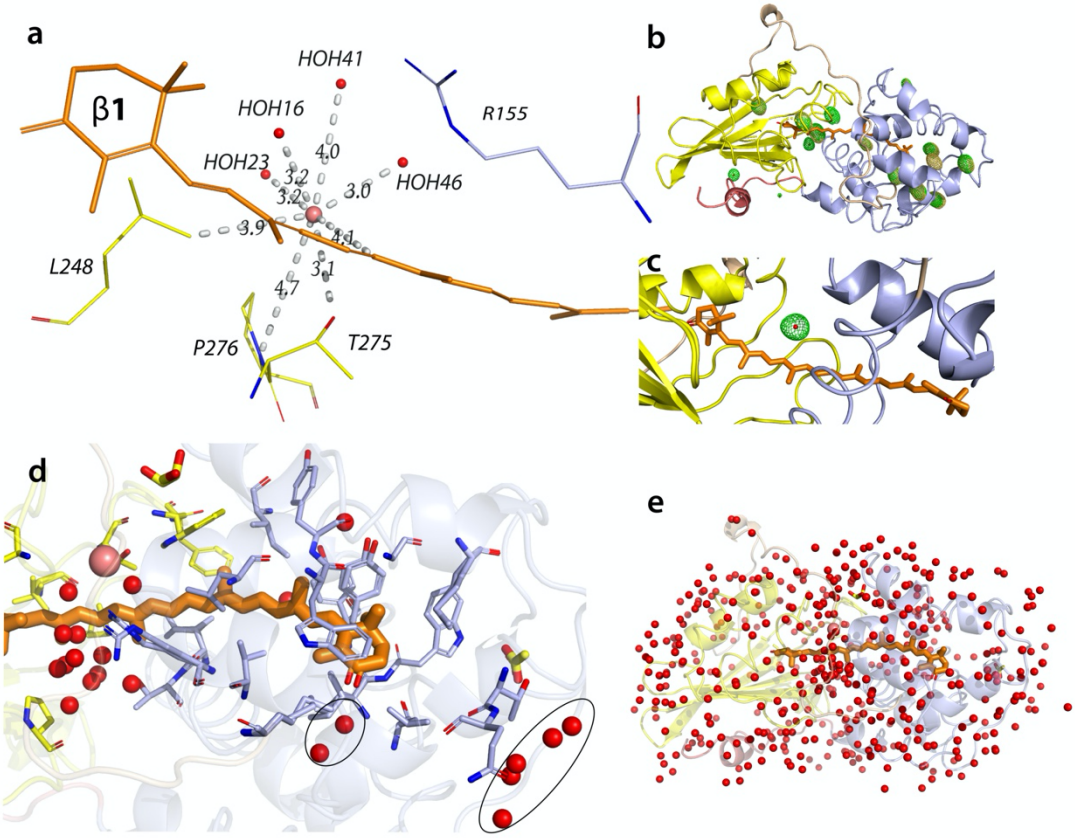

Extended Data Figure 1 Identifying Cl– location. (a) Cl- is resolved in the CTD using Long-wavelength experiment for Cl- identification. Cl- coordinates four water molecules through ion-dipole interactions at distances of 3.0-3.2 Å (HOH16, HOH23, HOH46) and 4.0 Å (HOH41). (b) Overall structure anomalous difference density Fourier maps at 2.9 keV (green) and 2.8 keV (light orange). The regions where green density is present and light orange density where it is absent indicate the presence of Cl (red dot). In the instances where the Cl atom could not be modelled due to a sigma greater than 6, dummy atoms have been placed to indicate the potential location (dots). (c) Close-up view of the modelled Cl- site (red dot) with the 2.9 keV anomalous difference Fourier map density surrounding it (green). (d) Zoomed view of the carotenoid tunnel with surrounding amino acids, water molecule (red spheres) and Cl^- ion (pink sphere) located within 6 Å of the carotenoid. The newly identified water molecules are highlighted within oval shapes (e) A total of 440 water molecules (red spheres) were resolved in the OCP structure reported herein.

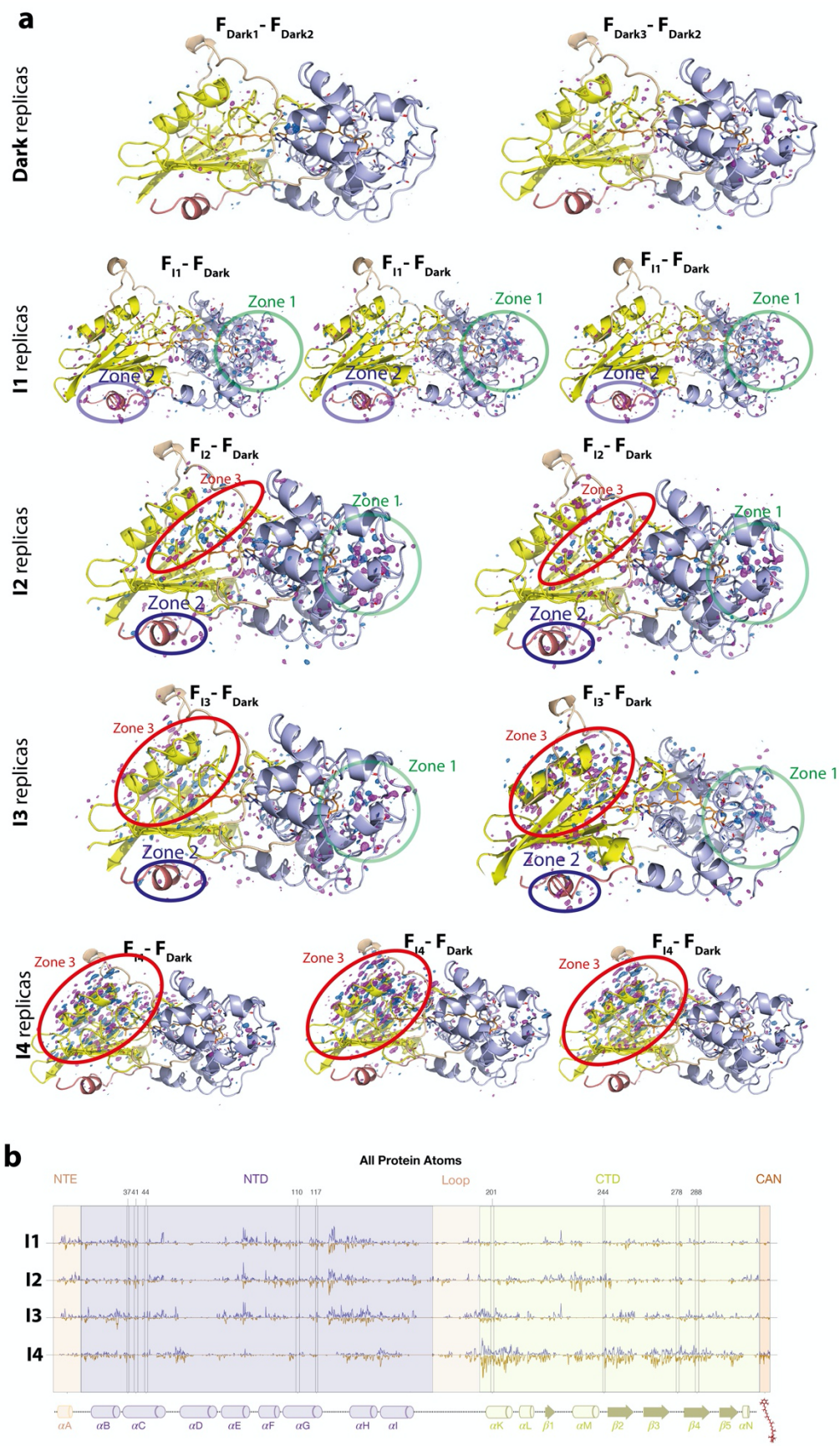

Extended Data Figure 2 (a) DED maps contoured at ±3.5σ (blue and magenta correspond to the appearance and disappearance of density, contoured at 3.5σ). Dark state DED signals contoured at (±)3.5σ The F_{Dark1}–F_{Dark2} and F_{Dark3}–F_{Dark2} exhibit marginal DED signals. The F_{I1}–F_{Dark}, F_{I2}–F_{Dark}, F_{I3}–F_{Dark} and F_{I4}–F_{Dark} datasets show reproducible strong DED signals in the three different zones. The following domains undergoing photoinduced conformational changes are represented in oval shapes: Zones 1 (NTD), Zones 2 (NTE) and Zones 3 (Alpha-helices in CTD) (b) Difference electron density amplitudes calculated as described in the X-ray crystallography and refinement section of the Materials and Methods.

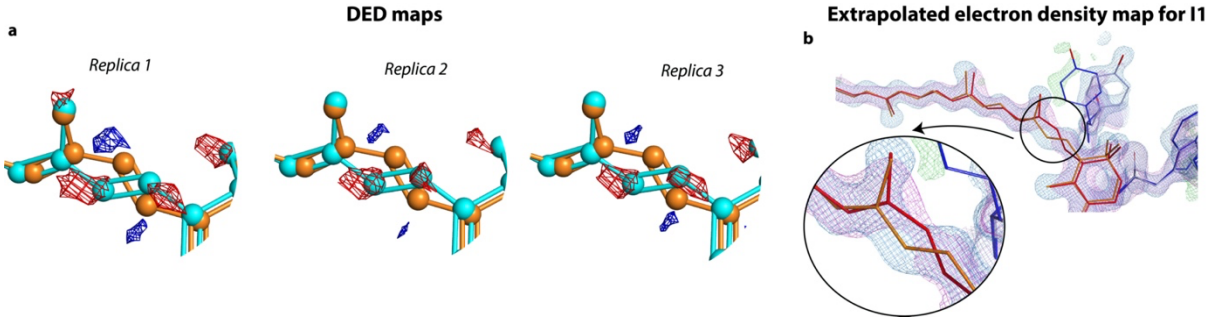

Extended Data Figure 3 Reproducibility of isomerization signal (a) Similar DED signals assigned to isomerization were observed for three different I1 datasets. (b) Extrapolated maps and coordinates of CAN.

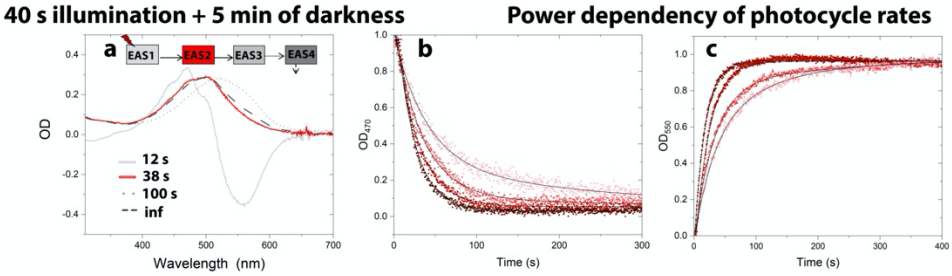

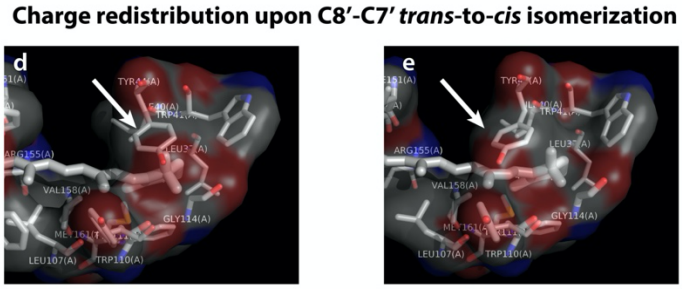

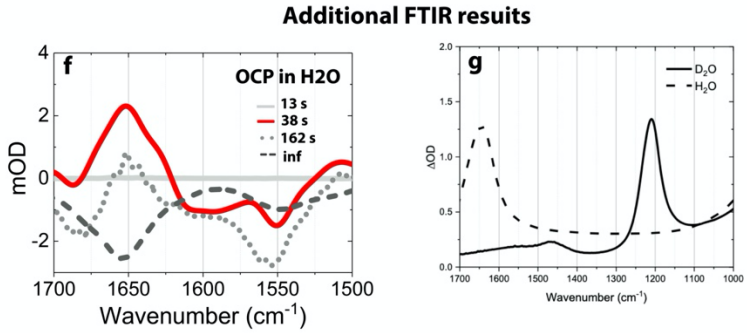

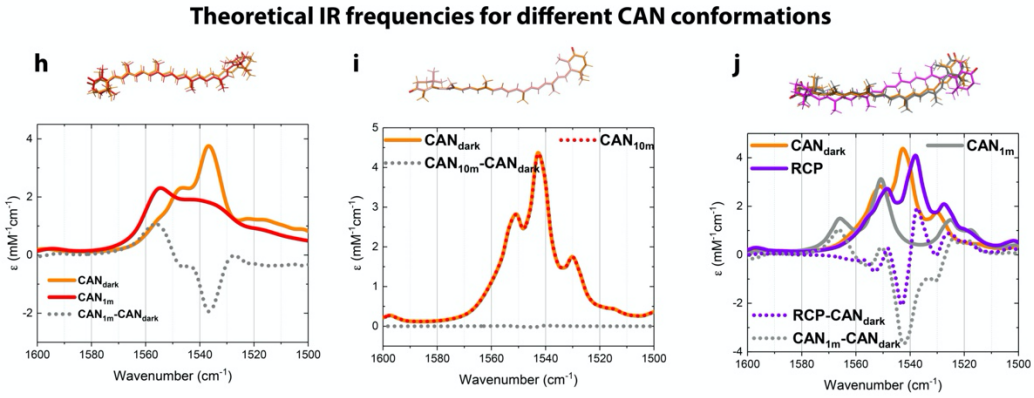

Extended Data Figure 4 (a) Results of the global fit of UV-VIS absorption kinetics upon 40 s of illumination followed by 5 min of darkness. The kinetic model used for the fit is indicated at the top of the graph (a) which also shows the lifetimes. (b and c) Power dependency profile of photocycle intermediate accumulation rates upon continuous illumination with violet light (410 nm) as monitored by 470 nm bleach (b) and 550 nm rise (c). Power densities used going from dark red to pink: 3.5 mW cm^{-2}, 2.8 mW cm^{-2}, 1.0 mW cm^{-2} and 0.5 mW cm^{-2}. Black lines represent double exponential fits of the curves. (d-e) Zoomed view of the carotenoid tunnel near the β2 ring in OCP_{Dark} (d)and OCP_{I1} (e) states. The *trans*-to-*cis*- C8'-C7' isomerization causes charge redistribution within the β2-binding pocket of the carotenoid. (f) Global analysis results obtained for OCP FTIR signals (H_2O) from the simultaneous global fit of UV-VIS/FTIR data. EAS1 shows no signal in IR region both in D_2O (Fig 4 a) and in H_2O. (g) FTIR spectra of H_2O (dashed line) and D_2O (solid line) alone. (h-j)Theoretical IR intensities were calculated using Harmonic frequency calculations (HFC) at the B3LYP/6-311+G level. (h) IR values were calculated for CAN in the two states CAN_{Dark} and CAN_{I1} when dihedral angles were freed in the calculation of the optimised geometry. (i) Calculated IR spectra for CAN_{dark} and CAN_{10m}. (j) Calculated IR spectra for CAN_{dark}, CAN_{1m} and RCP.

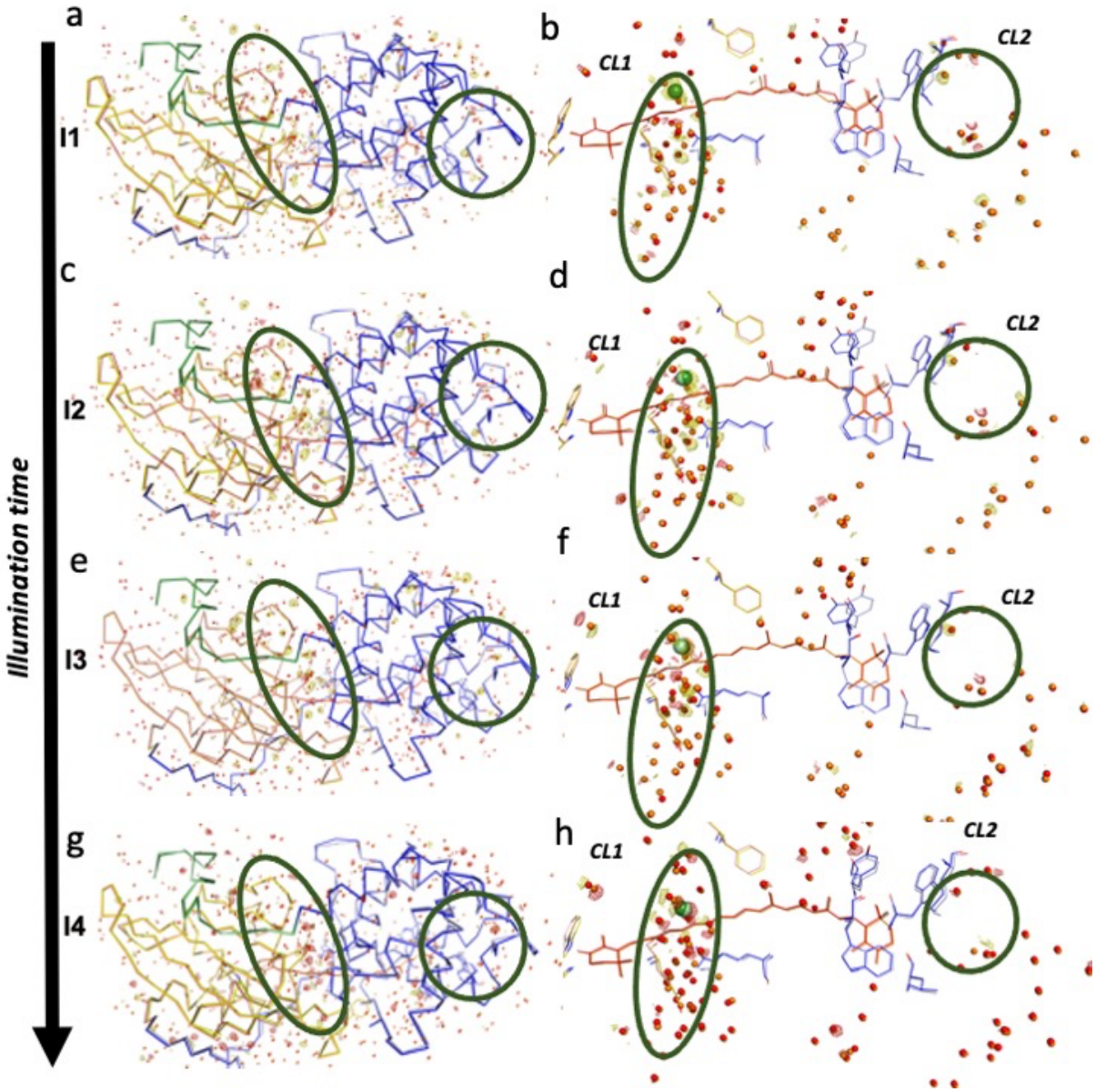

Extended Data Figure 5 Light-driven water molecules redistribution in the OCP crystal structures. Q-weighted DED maps obtained for the four pairs F_{I1}–F_{Dark}(a, b), F_{I2}– F_{Dark}(c,d), F_{I3} –F_{Dark}(e, f) and F_{I4} –F_{Dark} (g,h) (in yellow and red, contoured at ±3.0σ). CTD amino acids in dark and illuminated states are represented by yellow and deep salmon ribbons and sticks respectively. NTD amino acids in dark and illuminated states are represented by light and dark blue ribbons and sticks respectively. Water molecules present in OCP in dark and illuminated states are shown as orange and red spheres respectively. CL1 and CL2 indicate water clusters.

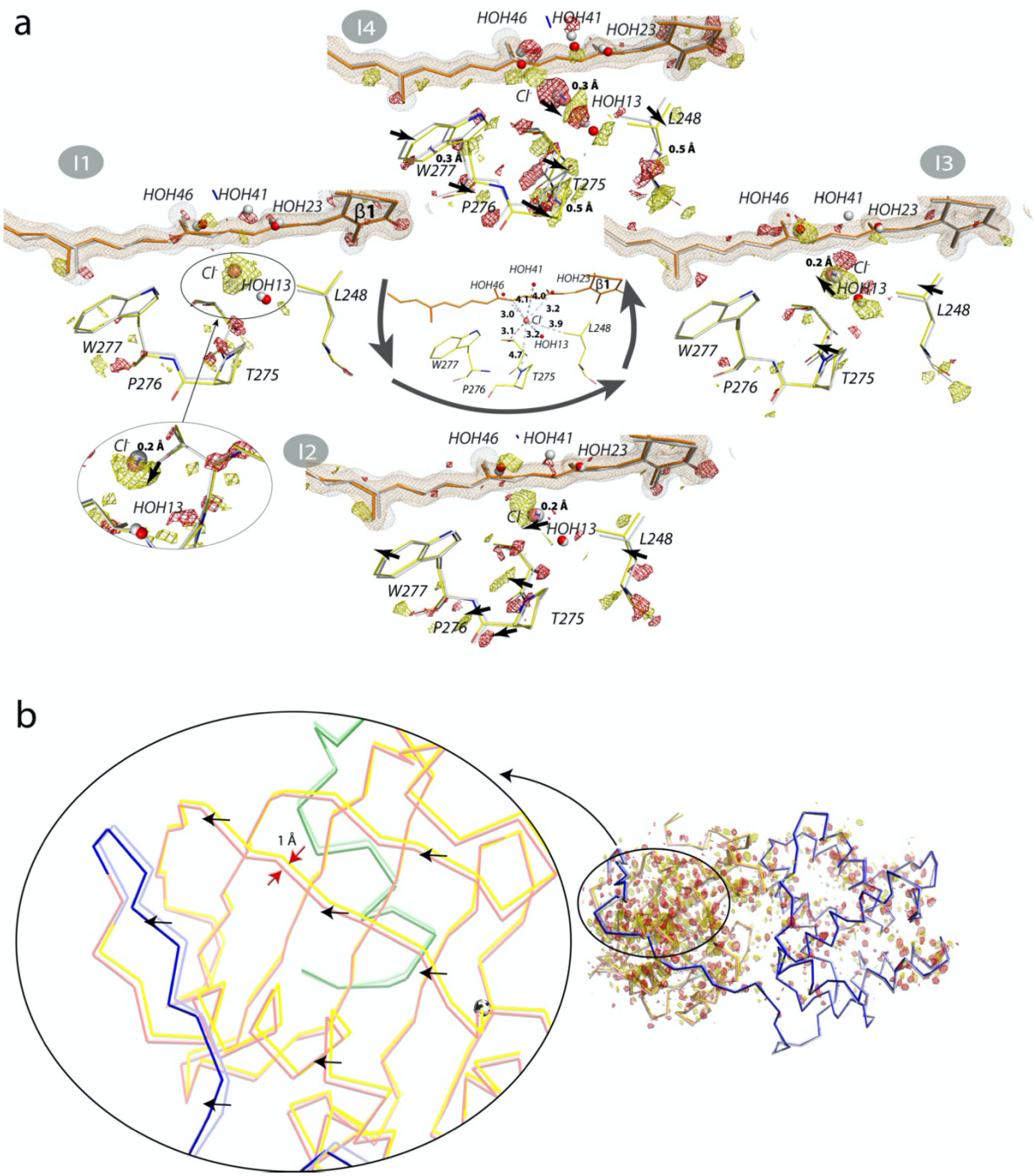

Extended Data Figure 6 (a) Light-driven structural changes in I1-I4 states. Features shown in oval shapes are within a 4 Å radius from the Cl^- ion. The grey and orange mesh represent the 2mFo-DFc maps of OCP in the dark and illuminated states contoured at 2.0σ. Dark state coordinates are shown in grey while light state coordinates are shown in yellow (CTD), blue (NTD), orange (CAN) and red spheres (HOH). F_{Light}–F_{Dark} DED contoured at ±3.0σ are shown in yellow and red mesh for the appearance and disappearance of density respectively. (b) Translocation of CTD from NTD in OCP_{I4}. DED maps obtained for F_{I4}–F_{Dark} (10 min) contoured at ±3.0σ (yellow and red for the appearance and disappearance of density respectively) and extrapolated coordinates for OCP_{I4} vs OCP_{Dark} showing a 1 Å translocation of CTD away from NTD.

Extended Data Table 1: Comparison of canthaxanthin dihedral angles observed in OCP structures in the three states: Dark, I1 (1 min of illumination) and I4 (10 min of illumination). Dihedral angles were measured using atomic PDB coordinates for carbon atoms. Deposited dihedral angles for CAN-binding (PDB entry 4XB5), ECN-binding (3MG1) and 3'-hECN-binding (1M98) OCPs are also included for comparison.

	Dark (this study)	**1m (this study)**	**10m (this study)**	**Syn OCP_{CAN} (4XB5)**	**Syn OCP_{ECH} (5TUX)**	**Syn OCP_{ECH} (3MG1 - CA)**	**Syn OCP_{ECH} (3MG1 - CB)**	**Arth OCP_{hECH} (5UI2 - CA)**	**Arth OCP_{hECH} (5UI2 - CB)**
C5-C6-C7-C8 (β1 ring)	153	157.8	-35.6	116.3	131.8	146.4	148.6	118.5	131.9
C6-C7-C8-C9	160	163.1	159.9	175.4	176.7	171	172.2	172.8	174.7
C7-C8-C9-C10	167	160.4	167	-155.3	-168.7	-179.5	179.5	-163.7	-176.8
C8-C9-C10-C11	164.9	162.4	164.9	175.8	174.9	169.3	170.9	177.9	171.1
C9-C10-C11-C12	-176.1	-166.1	-176.2	178.8	-179.5	173.2	173.5	165.2	173.6
C10-C11-C12-C13	176.9	-172.8	177.0	174.4	173.7	169.6	171.4	175.4	175.5
C11-C12-C13-C14	177.6	163	177.7	167.8	170	172.8	178	177.5	175.9
C12-C13-C14-C15	172.7	175.4	172.7	173	172.8	-177.3	-178.8	171	170
C13-C14-C15-C15'	175	-176.2	175	-171.4	177.8	-175.2	179.8	-175.7	171.5
C14-C15-C15'-C14'	172.4	144.9	172.4	172.7	171.8	168.7	167.7	170.7	171.4
C15-C15'-C14'-C13'	-175.2	163.8	-175.2	169.8	-178.7	178.9	178	179.6	-168.2
C15'-C14'-C13'-C12'	171.5	-177.5	171.5	173	172.2	170.9	170.4	172.8	169.8
C14'-C13'-C12'-C11'	-170.9	-148.1	-170.9	-153.3	-165.9	-172.4	-171.5	-161.6	171.4
C13'-C12'-C11'-C10'	172	171	172	173.1	172.8	171.4	171	174.8	170.9
C12'-C11'-C10'-C9'	-175.9	167.5	-175.9	171.9	-179.2	-177.3	-178.1	170.3	-158.8
C11'-C10'-C9'-C8'	172.9	173.3	172.8	175.2	174.8	174.2	174.6	174	-179.7
C10'-C9'-C8'-C7'	178.4	-23	178.3	-160.3	-175.1	-180	-179.4	-170.2	174.9
C9'-C8'-C7'-C6'	176.3	-171.6	176.3	177.6	178.5	177.2	176.8	177.3	178.6
C8'-C7'-C6'-C5' (β2 ring)	-45.3	145.1	-45.3	-72.1	-58.6	-52.7	-52.8	-66	-51.9

* Dihedral angles undergoing substantial change upon illumination are highlighted in grey.

Extended Data Table 2: Cl^- and water molecules located within 6 Å of the carotenoid. The molecules that are either conserved or found at the same location (within 0.5 A) as in previously reported OCP structures (PDB entries 4XB5, 5TUX, 5UI2) are indicated.

Name in PDB (current study)	B Factor	Nearest residue(s) that can form H bond	Distance, A	Corresponding molecule in 4XB5	Corresponding molecule in 5TUX	Corresponding molecule in 5UI2	Location and associated water cluster (CL1 or CL2 as in Fig S9)
HOH2	25.49 (A)/28.03 (B)	HOH217/O (A)/HOH93/O (B)	1.6(A)/1.7 (B)	HOH743	HOH756	HOH660	major interface/CL1
HOH23	23.26	HOH217/O and HOH385/O	2.1	HOH693	HOH602	HOH586	major interface/CL1
HOH30	25.77	TYR44/OH	2.3	HOH691	HOH505	No	TYR44
HOH46	27.35	ASN104/OD1	2.1	HOH699	HOH561	HOH561	major interface/CL1
HOH53	25.85	HOH256/O	2.5	No	No	No	between GLN36 and MET161
HOH57	23.43	No	No	HOH727	HOH577	HOH573	major interface/ CL1
HOH93	29.88	HOH2/O (B)	2.1	HOH728	HOH758	HOH661	major interface/CL1
HOH132	36.53	No	No	No	No	No	CL2, GLU34
HOH136	30.52	GLN228/NE2	2.7	HOH730	No	HOH535	major interface/CL1
HOH153	49.19	HOH421	1.9	HOH819	HOH521	No	major interface/CL1
HOH217	39.21	HOH2/O(A)	1.7	No	No	HOH647	major interface/CL1
HOH229	45.03	LEU77/O	2.7	No	No	No	CL2, LEU77
HOH250	42.7	HOH401/O	2.1	No	No	No	CL2, GLU250
HOH256	31.53	HOH53/O	2.2	No	No	No	CAN/O (keto group)
HOH320	64.68	No	No	No	No	No	MET47
HOH385	39.09	HOH2/O(A) and HOH424/O	1.8	HOH719	HOH720	No	major interface/ CL1
HOH401	49.9	HOH250/O	1.9	No	No	No	CL2, THR80
HOH420	56.95	HOH229/O	3	No	No	No	CL2, THR80
HOH424	67.81	HOH93/O	1.4	No	No	No	major interface/ CL1
HOH444	59.97	GLU244/OE1	1.2	No	HOH506	HOH504	major interface/ CL1
Cl	20.16	-	-	HOH673	HOH699	Cl	

Extended Data Table 3: X-ray crystallography data collection, refinement statistics and anomalous peaks for OCP. Statistics for the highest-resolution shell are shown in parentheses.

Energy	**2.9 keV**	**2.8 keV**	**Anomalous peaks**	**2.9 keV**			**2.8 keV**		
Wavelength (Å)	4.28	4.43		**Peak Height (σ)**	**Distance**	**Nearest Residue**	**Peak Height (σ)**	**Peak Height (σ)**	**Peak Height (σ)**
Resolution range	72 – 2.8 (2.95 – 2.8)	72 – 2.89 (3.07 – 2.89)		14.43	0.174	CYS245	12.9	12.9	12.9
Space group	$P3_221$	$P3_221$		14.18	0.14	MET202	12.6	12.6	12.6
Unit cell (Å, °)	82.67 82.67 87.58	82.660 82.660 87.580		14.12	0.502	MET161	12.07	12.07	12.07
	90 90 120	90 90 120		13.98	0.185	MET284	11.81	11.81	11.81
Total reflections	190330 (15166)	171371 (14952)		13.93	0.452	CL1	11.58	11.58	11.58
Unique reflections	8674 (1188)	7891 (1194)		13.35	0.144	MET74	11.54	11.54	11.54
Multiplicity	21.9 (12.8)	21.7 (12.5)		12.69	0.212	CYS95	11.32	11.32	11.32
Completeness (%)	98.3 (94.5)	98.0 (93.6)		11.56	0.167	MET83	10.73	10.73	10.73
Mean I/sigma(I)	18.9 (6.8)	14.6 (4.8)		11.32	0.152	MET117	9.32	9.32	9.32
Wilson B-factor	31.5	32.5		10.83	0.346	CYS84	7.7	7.7	7.7
R-merge	0.138 (0.304)	0.173 (0.413)		8.52	3.375	ASN285	6.01	6.01	6.01
R-meas	0.140 (0.316)	0.177 (0.429)		7.42	0.104	MET47			
R-pim	0.027 (0.082)	0.035 (0.111)		7.1	0.174	MET61			
CC1/2	0.998 (0.976)	0.997 (0.963)		7.06	0.802	ASN14			

*Cl anomalous peaks highlighted in green.

Extended Data Table 4: Light-driven newly formed H-bonds in the NTD main chain. The H-bond list was obtained using the list_mc_hbonds.py script from Robert L. Campbell (http://pldserver1.biochem.queensu.ca/~rlc/work/pymol/). Water molecules were excluded from the calculations.

		Distances, Å			
H-bond (inter subunit only)		I1	I2	I3	I4
A/ILE`25/N	A/PRO`22/O	3.45	3.39		
A/ARG`27/N	A/THR`24/O	3.53	3.38	3.26	
A/LEU`37/N	A/GLU`34/O	3.35	3.32		3.29
A/ALA`38/N	A/ASP`35/O	3.35	3.34		
A/THR`52/N	A/THR`52/O	3.09			
A/SER`60/N	A/GLY`57/O	3.05	3.2	3.14	
A/GLU`65/N	A/LEU`63/O	3.66	3.61		
A/LYS`69/N	A/ASN`66/O	3.72	3.59	3.33	3.36
A/CYS`84/N	A/GLN`81/O	3.31	3.27		3.22
A/ALA`87/N	A/CYS`84/O	3.00	3.09	3.28	
A/TYR`98/N	A/CYS`95/O	3.39		3.51	3.55
A/LYS`106/N	A/PRO`103/O	3.18	3.32		
A/TYR`111/N	A/GLY`108/O	3.24	3.28	3.28	3.51
A/LEU`113/N	A/TRP`110/O	3.64	3.45	3.26	3.43
A/ALA`140/N	A/ALA`137/O	3.23	3.33	3.32	3.37

* The pattern of newly formed and disrupted hydrogen bonds between intermediates illustrates the transient nature of the hydrogen bonding and agrees with our FTIR results (Fig 4). Out of 15 hydrogen bonds, most remain in the I1 and I2 structural intermediates, 7 do so in I1-I3 while 4 remain in all intermediates.